

DAM-BREAK REFLECTION

by ANDREW J. HOGG[†] and EDWARD W.G. SKEVINGTON

(School of Mathematics, University of Bristol, Woodland Road, Bristol BS8 1UG, UK)
(Energy and Environment Institute, University of Hull, HU6 7RX, UK.)

[Received 6 July 2021 Revised 2 August 2021 Accepted 3 August 2021]

Summary

The unsteady reflection of dam-break flow along a horizontal channel by a remote barrier is modelled using the nonlinear shallow water equations. The interaction generates an upstream moving bore that connects the collapsing reservoir of fluid to a rapidly deepening fluid layer adjacent to the barrier. These motions are modified when the fluid is released into a channel containing a pre-wetted layer, because the oncoming flow is itself headed by a bore that alters the initial reflection. Solutions for these flows are calculated using quasi-analytical techniques that utilise the method of characteristics and the hodograph transformation of the governing equations, and the results are validated by comparison with direct numerical integration of the shallow water equations. The analytical solutions enable the precise identification of dynamical features in the flow, including the onset and development of discontinuous solutions that are manifest as bores, as well as their long term behaviour, the rate at which energy is dissipated, and for flows generated from the release of a finite reservoir, the maximum depth of the fluid layer at the barrier.

1. Introduction

Dam-break flows, which arise following the instantaneous removal of a lockgate confining a reservoir of quiescent fluid, have been studied in many situations. Not only is this form of unsteady and spatially varying motion readily generated in the laboratory (1–3), but it also provides important insight to large-scale geophysical and environmental flows (see, for example, (4) for an analysis of the 1923 Gleno dam-break in the central Italian alps). Mathematically, the motion is often modelled using the nonlinear shallow water equations, which are applicable once the flow has become sufficiently ‘shallow’, so that fluid flows predominantly parallel to the underlying bed, its vertical component of fluid acceleration is negligible and the pressure is hydrostatic to leading order. Ritter (5) derived the solution for dam-break flow of a semi-infinite reservoir into a horizontal, two-dimensional (2D) channel that is initially fluid-free, and several subsequent studies have used this fundamental solution as a building block for investigating additional effects. Examples include the investigation of the unsteady collapse of a reservoir of fluid into a channel that initially contains a non-vanishing, motionless layer of fluid (6); the influence of hydraulic resistance on the motion (7, 8); the effects of a finite reservoir of fluid (9); and motion along an inclined channel (10). In all of these problems, the governing equations and boundary conditions remain straightforward, but the calculation of the ensuing unsteady motion is non-trivial.

In this contribution, we calculate the reflection of the oncoming dam-break flow by a rigid, impermeable and immovable barrier. A reflected bore (‘shock’) is generated by the interaction with

[†]Corresponding author <a.j.hogg@bris.ac.uk>

the barrier, and propagates upstream. Between the bore and the barrier, the fluid forms a progressively deepening layer, the depth of which asymptotes to the original depth of fluid in the reservoir, when the reservoir is of infinite extent. The flow velocities downstream of the bore are relatively small (and vanish at the barrier). We calculate the complete unsteady flow fields; in particular, there are two key outcomes, namely the determination of the position of the upstream-moving shock and the growing depth of the fluid layer adjacent to the barrier. The former reveals how the upstream conditions are progressively modified by reflection, whereas the latter determines the growing hydrostatic force on the barrier and the associated potential for overtopping or damage.

The interaction between unsteady hydraulic flows and structures has been the focus of recent research activities, driven in part by the need to evaluate flood-induced damage to structures and the efficacy of preventative measures. Dam-break flows are often used as a configuration in which this interaction may be examined, because they are readily set-up in the laboratory and numerical experiments, and yet exhibit sufficient complexity and similarity to naturally occurring flows to enable deductions about processes at environmental scales. Measurements have been reported of the flow depths following reflection, measured at discrete locations (11, 12), velocity fields deduced from particle-image-velocimetry (12, 13) and dynamic pressure and force loads on objects (13–15). These investigations includes flows reflected by channel width-filling objects (11–13, 16), the deflection around isolated objects (14, 15, 17) and the motion through ensembles of objects, or ‘cities’, (18). The approaches to modelling the interactions between the fluid and the structures have also varied in complexity, including three-dimensional simulations of the Navier–Stokes equations, Reynolds-averaged equations and the nonlinear shallow water equations (see, for example, (14)). Additionally some studies have accounted for multiphase flows by modelling the entrainment of air and the transport of suspended sediment (19, 20). Lobovsky *et al.* (13), amongst others, show that the early stages of the interaction creates significant vertical velocities. These processes are not-captured by the shallow water equations which are based upon the assumption of negligible vertical accelerations of fluid. However, at later times, Aureli *et al.* (14) find that the force exerted by the motion is adequately represented by a shallow water model, as the flow deepens to generate a growing hydrostatic pressure. Dam-break release and interaction with barriers have also been analysed in the context of bunds, which are intended to confine releases of hazardous materials (21–23). In that scenario the bund could be overtopped by the oncoming fluid. Overtopping is not the focus of this work; instead the fluid motion is completely reflected. However, elucidating the state of the flow prior to overtopping is another important application of our calculations, and moreover, we show our calculations may be used to evaluate the maximum depth from a flow released from a reservoir of finite extent.

Our methods employ both analytical techniques, using the hodograph transformation of the shallow water equations and direct numerical integration. Hodograph techniques yield precise quasi-analytical results for unsteady hydraulic flows and provide significant insight into the ensuing fluid motions. Flows analysed using these methods have included unsteady collapses of finite length reservoirs into 2D channels (24); the run-up of swash on an inclined planar beach and the formation of the backwash bore (25); and the collapse of a fluid reservoir over a weir and through a constriction (26). Although the hodograph techniques appear cumbersome at first sight, the approach permits the quasi-analytical solution of complicated flows and the precise identification of the onset and evolution of shocks and locations at which the gradients of the dependent variables are discontinuous. These features are challenging to compute accurately in simulations of the shallow water equations, and yet for the flows examined in this study, such effects play a vital role in the motion. For the same problems as those tackled analytically, we also present results from the direct numerical integration of the

governing equations; these new results employ central schemes for nonlinear systems of hyperbolic equations developed by (27). We show that there is excellent agreement between the analytical and numerical approaches, including tracking the development of discontinuities. In addition, we comment that the new analytical results provide a series of severe tests of all numerical methods that have been developed to compute flows of this nature.

The reflection of a dam-break release into an initially dry channel, modelled using the shallow water equations, was analysed by (21) and has a counterpart in the reflection of a polytropic gas by a planar boundary, a problem that was tackled by (28) and (29). These classical studies share some of the same structure of solution with section 3 and feature an initial release that corresponds to a rarefaction (or ‘simple’ wave), and a reflected bore. The analyses deployed by (28, 29) and (21) are, however, limited to relatively early times after the first interaction with the boundary so that the flow upstream of the bore only weakly varies from its form when the bore first arises. This differs from our focus, which is to compute the complete solution for all times. However, we also include Appendix A in which we derive the solution as a series expansion that is formally valid for relatively early times. By expanding in terms of a nonlinear function of time, our series solution improves upon (21) by remaining close to the full solution over a longer temporal range.

The paper is organised as follows. First in section 2, we present the formulation of the model, our analytical and numerical techniques, and review the collapse of the initially motionless reservoir before reflection. The canonical problem of dam-break reflection when the channel is initially free of fluid is analysed in section 3 to reveal the upstream velocity of the bore and the spatial and temporal dependence of the deepening fluid layer between the bore and the reflecting barrier. When the channel contains a pre-existing layer of stationary fluid known as a ‘tailwater’, the reflection is more complicated because the oncoming motion is itself headed by a shock that is reflected upstream. This scenario is analysed in section 4, extending the canonical problem of section 3 and including comparison with experimental data. Dissipation in flows with and without a tailwater only occurs at the shock and is analysed in section 5. For releases from reservoirs of finite length, the fluid depth at the barrier initially increases, but reaches a maximum after a finite time. We show in section 6 how the maximum depth, and the time at which it is attained, may be evaluated straightforwardly using the solution developed here. Brief concluding comments are given in section 7. Our contribution also includes Appendix A, in which we develop a new series solution for the initial stages of the reflection of dam-break flow when the channel is fluid-free.

2. Governing equations

We model the 2D, unsteady gravitational collapse of initially quiescent fluid within a semi-infinite reservoir of fluid of depth H as it flows horizontally and is reflected by an immobile barrier located downstream at distance $2L$ from the lockgate (see Fig. 1 for a sketch of the configuration of the flow). The fluid motion is modelled on the assumptions that the flow is shallow ($H/L \ll 1$) and the pressure hydrostatic to leading order. Thus, the governing equations are the dimensionless, nonlinear shallow water equations given by

$$\frac{\partial h}{\partial t} + \frac{\partial}{\partial x}(uh) = 0, \quad (2.1)$$

$$\frac{\partial u}{\partial t} + u \frac{\partial u}{\partial x} + \frac{\partial h}{\partial x} = 0. \quad (2.2)$$

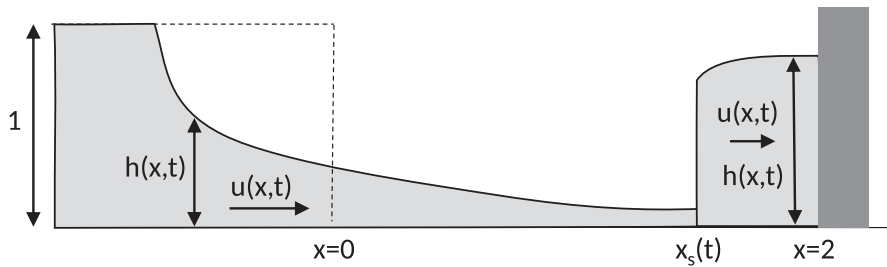


Fig. 1 The flow configuration for dam-break reflection by a barrier and the dimensionless variables used to model the motion. The fluid is instantaneously released from a reservoir depicted with a dashed line.

(see, for example, (30)). In these expressions we have non-dimensionalised the depth of the flowing layer, $h(x, t)$, by the initial depth of fluid in the reservoir, H ; the velocity of the fluid layer, $u(x, t)$, by $(gH)^{1/2}$, where g denotes gravitational acceleration; horizontal distances, x , by L and times, t , by $L/(gH)^{1/2}$. Viscous stress are assumed negligible (i.e. $\rho(gH^5)^{1/2}/(L\mu) \gg 1$, where ρ and μ denote the density and dynamic viscosity of the fluid, respectively).

The shallow water equations ((2.1) and (2.2)) are hyperbolic and may be written in terms of quantities $\alpha = u + 2h^{1/2}$ and $\beta = u - 2h^{1/2}$, which are invariant along characteristics (31). Thus the governing equations in characteristic form are given by

$$\frac{d\alpha}{dt} = 0 \quad \text{on} \quad \frac{dx}{dt} = u + h^{1/2} \quad \text{and} \quad \frac{d\beta}{dt} = 0 \quad \text{on} \quad \frac{dx}{dt} = u - h^{1/2}. \quad (2.3)$$

The solutions exhibit regions in which the characteristic functions (α and β) are both constant, one of them is constant, or both vary. These are termed uniform regions, simple wave regions and complex wave regions respectively, and this demarcation and terminology helps to elucidate the dynamical behaviour. The equations may also exhibit discontinuous solutions. We enforce jump conditions that balance the mass and momentum fluxes across a discontinuity at $x = x_s(t)$, moving with streamwise velocity $c \equiv dx_s/dt$ (31). Using $[\dots]_{-}^{+}$ to denote the change in value across the discontinuity, we impose the jump conditions

$$[(u - c)h]_{-}^{+} = 0 \quad \text{and} \quad \left[(u - c)^2 h + \frac{1}{2} h^2 \right]_{-}^{+} = 0. \quad (2.4)$$

The initial conditions are that the fluid is at rest throughout, $u(x, 0) = 0$, and that the fluid is of unit dimensionless depth upstream of the dam at $x = 0$, namely $h(x, 0) = 1$ for $x \leq 0$. Downstream of the dam, there is a uniform wetting layer (often termed the ‘tailwater’), $h(x, 0) = h_0$ for $x > 0$, where $0 \leq h_0 < 1$. When $h_0 = 0$, the fluid intrudes into a dry channel and the flow problem without the downstream barrier corresponds to the classical dam-break flow (5). When $h_0 > 0$, the flow problem is known as the ‘Stoker problem’ (6).

The boundary condition is that the barrier is immovable and not overtopped,

$$u(2, t) = 0. \quad (2.5)$$

2.1 Initial motion before reflection

The initial motion before interaction with the barrier is easily constructed using the characteristics of the system (2.3) and corresponds to a rarefaction fan of β -characteristics centred on $x = 0$, upstream of which the fluid is undisturbed from the quiescent conditions in the reservoir ($u = 0, h = 1$) and downstream of which there is a region within which the depth and velocity fields are uniform. This latter region connects to the tailwater via a shock (6). The α -characteristics are forward propagating and those which start from the reservoir ($x < 0$) correspond to $\alpha = 2$. Thus, it is straightforward to construct the complete solution

$$h = \begin{cases} 1, & x/t < -1, \\ \frac{1}{9}(2 - x/t)^2, & -1 < x/t < V_1, \\ \frac{1}{16}(2 - \beta_*)^2, & V_1 < x/t < V, \\ h_0, & V < x/t, \end{cases} \quad \text{and} \quad u = \begin{cases} 0, & x/t < -1, \\ \frac{2}{3}(1 + x/t), & -1 < x/t < V_1, \\ \frac{1}{2}(2 + \beta_*), & V_1 < x/t < V, \\ 0, & V < x/t, \end{cases} \quad (2.6)$$

where $\beta = \beta_*$ on the lead β -characteristic from the fan, which advances with velocity $V_1 = (3\beta_* + 2)/4$ and V is the velocity of the shock that joins the collapsing flow to the tailwater. Denoting the depth and velocity of the fluid upstream of the shock by $h_f = (2 - \beta_*)^2/16$ and $u_f = (2 + \beta_*)/2$, respectively, the shock conditions (2.4) lead to

$$2h_0u_f^2h_f = (h_0 + h_f)(h_f - h_0)^2, \quad (2.7)$$

and thus β_* (and V and V_1) are determined as a function of the tailwater depth. In what follows we often illustrate the reflected Stoker solution for the cases $V_1 = 0$, which corresponds to $h_0 = 0.1383$, or $V_1 = 1/2$, which corresponds to $h_0 = 0.0275$, or we specialise to the case of vanishing tailwater ($h_0 = 0$).

There is relatively strong dependence on h_0 . We can show that when $h_0 \ll 1$

$$V = 2 - 2^{7/4}h_0^{1/4} + \dots, \quad V_1 = 2 - 3 \times 2^{3/4}h_0^{1/4} + \dots \quad (2.8)$$

$$h_f = 2^{3/2}h_0^{1/2} + \dots, \quad u_f = 2 - 2^{7/4}h_0^{1/4} + \dots \quad (2.9)$$

In the limit of a dam-break collapse into a dry channel, we note that there is no longer a shock at the front of the motion and no longer a region within which the velocity and depth are uniform ($V, V_1 \rightarrow 2$ and $h_f \rightarrow 0$ as $h_0 \rightarrow 0$). Instead the initial motion is just a rarefaction fan. The interaction of the dam-break flow with a barrier for this case is therefore simpler to analyse and this will be undertaken first (section 3), before deriving results for the more complex Stoker problem (section 4).

2.2 Hodograph techniques

Given the hyperbolic structure of the governing equations, it is possible to interchange the dependent and independent variables to treat x and t as real-valued functions of the characteristic invariants, α and β , provided the Jacobian of the transformation remains finite and non-vanishing. This transformation converts the nonlinear governing equations into linear equations and allows significant analytical progress in determining the nonlinear solution to the original equations ((2.1) and (2.2)).

In particular as shown by Hogg (9), the characteristic equations (2.3) are now given by

$$\frac{\partial x}{\partial \beta} = \frac{(3\alpha + \beta)}{4} \frac{\partial t}{\partial \beta} \quad \text{on} \quad \alpha = \text{constant}, \quad (2.10)$$

$$\frac{\partial x}{\partial \alpha} = \frac{(\alpha + 3\beta)}{4} \frac{\partial t}{\partial \alpha} \quad \text{on} \quad \beta = \text{constant}. \quad (2.11)$$

The fundamental solution to the adjoint governing equation, termed the Riemann function, can then aid the construction of the solution from conditions along boundaries in the hodograph plane, (α, β) . This technique has been used by Hogg and coworkers to solve gravity current and hydraulic problems using quasi-analytical techniques (9, 24, 25, 32). The Riemann function is given by (33)

$$B(a, b; \alpha, \beta) = \frac{(a-b)^3}{(a-\beta)^{3/2}(\alpha-b)^{3/2}} \mathcal{F} \left[\frac{3}{2}, \frac{3}{2}; 1; \frac{(a-\alpha)(\beta-b)}{(a-\beta)(\alpha-b)} \right], \quad (2.12)$$

where \mathcal{F} denotes the hypergeometric function. Integration around a closed curve, $\partial \mathcal{D}$, in the hodograph plane yields

$$\int_{\partial \mathcal{D}} -V da + U db = 0, \quad (2.13)$$

with

$$U = -\frac{3}{2(a-b)} tB + \frac{B}{2} \frac{\partial t}{\partial b} - \frac{t}{2} \frac{\partial B}{\partial b} \quad \text{and} \quad V = \frac{3}{2(a-b)} tB + \frac{B}{2} \frac{\partial t}{\partial a} - \frac{t}{2} \frac{\partial B}{\partial a}, \quad (2.14)$$

where the dependent variable t and its derivatives are evaluated at a and b . In terms of hodograph variables and using (2.10) and (2.11), the boundary condition (2.5) corresponds to

$$\frac{\partial t}{\partial \alpha} + \frac{\partial t}{\partial \beta} = 0 \quad \text{on} \quad \alpha + \beta = 0. \quad (2.15)$$

The method of characteristics and the hodograph transformation are used extensively in this study. Although the analytical machinery of the hodograph transformation may seem cumbersome, the final equations exploit the linearity of (2.10) and (2.11) and enable rapid and accurate computation of results. This makes it straightforward to identify the behaviour of shocks and other discontinuities, which are difficult to identify precisely from the direct numerical integration of the governing equations.

2.3 Numerical method

We also directly numerically integrate the system of equations (2.1)-(2.2) using a central upwind scheme (27) on a uniform grid of 10^4 cells with domain $-t < x < 2$, imposing non-reflecting conditions at $x = -t$ and (2.5) at $x = 2$. Numerical reconstruction of the dependent variables is performed with the modified minmod limiter proposed in (34) which suppresses oscillations around slowly moving shocks, using the parameters selected for their test problems. The boundary conditions and time evolving domain are implemented using the approach developed in (35), again with the parameters selected for their test problems. The time stepping algorithm is the second-order, total-variation-diminishing (TVD) algorithm from (36), using the modified Euler time steps from the 'RKNR' scheme developed in (35), which eliminates drift-off error in the algebraic boundary conditions. The numerical simulations will be shown to be in excellent agreement with the quasi-analytical hodograph results, supporting the accuracy of both approaches.

while the velocity of the shock satisfies

$$\frac{dx_s}{dv} = c \frac{dt_s}{dv}. \quad (3.2)$$

The depth of the fluid layer and its velocity upstream of the shock ($x = x_s^-$) are given by (2.6) and may be written as

$$h = h^- \equiv (\nu/4)^2 \quad \text{and} \quad u = u^- \equiv 2 - \nu/2. \quad (3.3)$$

The shock is initiated at the barrier when the lead characteristic ($\nu = 0$) reaches $x = 2$ at $t = 1$. Thus, we have $x_s(0) = 2$, $t_s(0) = 1$ and $c(0) = 0$. The latter condition follows by balancing the volume and momentum fluxes across the shock at early times (see Appendix A). Combining (3.1) and (3.2), yields

$$\frac{dt_s}{dv} = \frac{3t_s}{8 - 4c - 3\nu}. \quad (3.4)$$

Immediately downstream of the shock ($x = x_s^+$), the flow satisfies $h = h_s$ and $u = u_s$, which together determine the characteristic variables $\alpha_s = u_s + 2\sqrt{h_s}$ and $\beta_s = u_s - 2\sqrt{h_s}$. Then (3.2) using the variables downstream of the shock ($x_s \equiv x(\alpha_s, \beta_s)$, $t_s \equiv t(\alpha_s, \beta_s)$) may be written

$$\frac{\partial x_s}{\partial \alpha} \frac{d\alpha_s}{dv} + \frac{\partial x_s}{\partial \beta} \frac{d\beta_s}{dv} = c \left(\frac{\partial t_s}{\partial \alpha} \frac{d\alpha_s}{dv} + \frac{\partial t_s}{\partial \beta} \frac{d\beta_s}{dv} \right). \quad (3.5)$$

Using (2.10) and (2.11), this leads to

$$\frac{4}{\alpha_s - \beta_s} \left(c - \frac{(\alpha_s + \beta_s)}{2} \right) \frac{dt_s}{dv} = \frac{\partial t_s}{\partial \beta} \frac{d\beta_s}{dv} - \frac{\partial t_s}{\partial \alpha} \frac{d\alpha_s}{dv}. \quad (3.6)$$

This expression will be used to simplify some of the path integrals in the hodograph plane.

The jump conditions (2.4) can be manipulated to determine the flow state downstream of the shock, u_s and h_s , in terms of the state upstream given by (3.3), and the shock velocity, c . Thus, we find

$$h_s = \frac{h^-}{2} \left(\left(1 + \frac{8(u^- - c)^2}{h^-} \right)^{1/2} - 1 \right) \quad \text{and} \quad u_s = c + (u^- - c) \frac{h^-}{h_s}. \quad (3.7)$$

These expressions (3.7) therefore determine the characteristic functions, α_s and β_s (and their derivatives with respect to ν) in terms of the parameter ν and the as yet undetermined shock velocity, c .

The final stage of the analysis is to determine useful curves in the hodograph plane around which to integrate (2.13) and to use these integrals to determine the shock velocity. We note that the solution upstream of the shock is a simple wave, which corresponds to the line $\alpha = 2$ in the hodograph plane for $-2 \leq \beta \leq 2$, which is equivalent to $0 \leq \nu \leq 4$ (see Fig. 3). The jump conditions map locations on this line to the shock curve given parametrically by (α_s, β_s) . The motion downstream of the shock, which is C_1 in the characteristic plane, corresponds to the region in the hodograph plane between the shock curve and $\alpha = -\beta$. The shock curve is initiated at the origin of the hodograph plane $(\alpha_s, \beta_s) = (0, 0)$

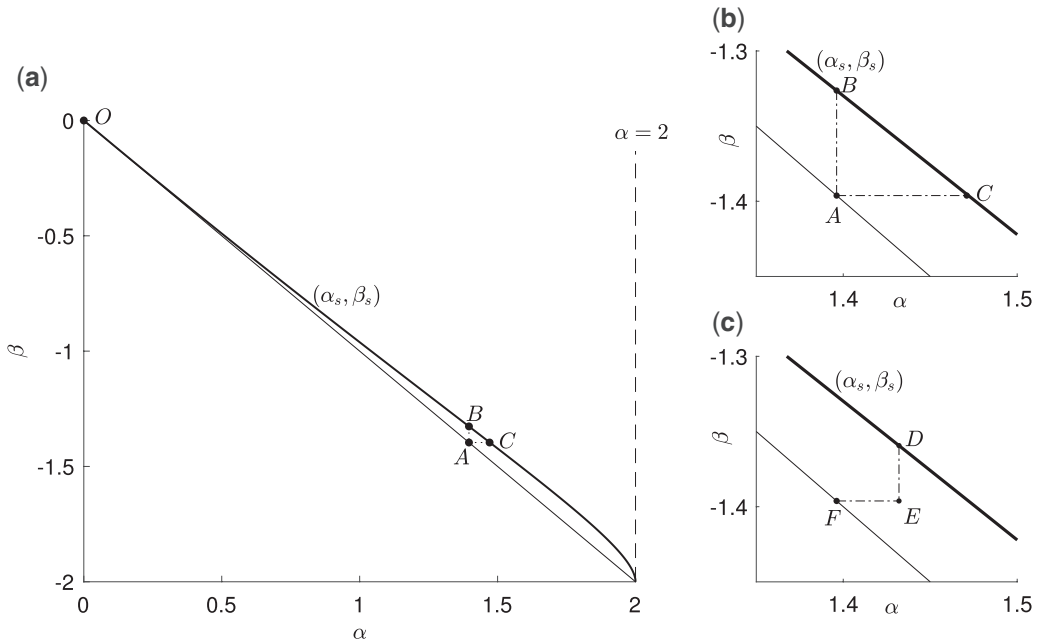


Fig. 3 (a) The hodograph plane, featuring the initial motion within simple wave region S_1 in which $\alpha = 2$, the impermeable barrier at $x = 2$, on which $\alpha = -\beta$, the trajectory of the shock curve (α_s, β_s) (thick line) and the points O, A, B and C used in (3.11) and (3.12); (b) zoomed in view of the points A, B and C ; (c) zoomed in view of points D, E and F used in (3.15).

and at long times the shock approaches the most rapidly rearward-moving β -characteristic, on which $\beta = -2$ (see section 5). Thus, we deduce that $c \rightarrow -1$ and $(\alpha_s, \beta_s) \rightarrow (2, -2)$ as $v \rightarrow 4$.

We integrate (2.13) around two closed curves in the hodograph plane, namely OAC and OAB (see Fig. 3). The curve segments BO and CO both lie on the shock curve (α_s, β_s) , the line segment OA along $\alpha = -\beta$, the line AB along the $\alpha = \alpha_s(v_B)$ characteristic, and the line AC along the $\beta = \beta_s(v_C)$ characteristic, where

$$\alpha_s(v_B) + \beta_s(v_C) = 0. \tag{3.8}$$

This ensures that the β -characteristic, AC , intersects the α -characteristic, AB , at $\alpha + \beta = 0$. The coordinates of these points in the hodograph plane are given by: $O = (0, 0)$; $A = (\alpha_s(v_B), -\alpha_s(v_B))$; $B = (\alpha_s(v_B), \beta_s(v_B))$; and $C = (\alpha_s(v_C), \beta_s(v_C))$ with $v_C > v_B$. Both closed curves OAB and OAC involve integrating along the parameterised shock curve, which entails evaluating

$$I(v_*; v_0) = \int_{v_*}^{v_0} -Va'_s + Ub'_s \, dv, \tag{3.9}$$

where $v_* = v_C$ for CO , $v_* = v_B$ for BO , $v_0 = 0$ in this scenario of no tailwater, the functions a_s and b_s parameterise the path as functions of v and a prime denotes differentiation with respect to v . Substituting for V and U from (2.14) and then using (3.4) and (3.6) to simplify the expressions, we

find that

$$I(\nu_*; 0) = \int_{\nu_*}^0 \frac{3t_s B}{2(a_s - b_s)} \left(\frac{c - \frac{1}{2}(a_s + b_s)}{(2 - \frac{3}{4}v - c)} - (a'_s + b'_s) \right) + \frac{t_s}{2} \left(\frac{\partial B}{\partial a} a'_s - \frac{\partial B}{\partial b} b'_s \right) d\nu \quad (3.10)$$

In this integral the Riemann function, B , and its derivatives are evaluated at $a = a_s(\nu)$, $b = b_s(\nu)$, $\alpha = \alpha_s(\nu_B)$ and $\beta = -\alpha_s(\nu_B)$.

We may now evaluate the integral (2.13) around the curve OAB and simplify using boundary condition (2.15), which yields

$$0 = \left(\frac{\alpha_s(\nu_B) - \beta_s(\nu_B)}{2\alpha_s(\nu_B)} \right)^{3/2} t_s(\nu_B) - t_w(\nu_B) + 2I(\nu_B; 0), \quad (3.11)$$

while from the curve OAC , we find

$$0 = - \left(\frac{\alpha_s(\nu_C) - \beta_s(\nu_C)}{2\alpha_s(\nu_B)} \right)^{3/2} t_s(\nu_C) + t_w(\nu_B) + 2I(\nu_C; 0). \quad (3.12)$$

In expressions (3.11) and (3.12), $t_w(\nu) \equiv t(\alpha_s(\nu), -\alpha_s(\nu))$ and denotes the time at the impermeable barrier ($x = 2$) as a function of the parameter ν . Summing (3.11) and (3.12) eliminates t_w and gives

$$\left(\frac{\alpha_s(\nu_B) - \beta_s(\nu_B)}{2\alpha_s(\nu_B)} \right)^{3/2} t_s(\nu_B) - \left(\frac{\alpha_s(\nu_C) - \beta_s(\nu_C)}{2\alpha_s(\nu_B)} \right)^{3/2} t_s(\nu_C) = -2(I(\nu_C; 0) + I(\nu_B; 0)). \quad (3.13)$$

This is a single integral equation in which the shock velocity, c , and its derivative, $dc/d\nu$, are the only unknowns.

We proceed by finding a numerical solution for $c(\nu)$ in the range $\nu_0 \leq \nu \leq 4$ that satisfies (3.13) using pseudo-spectral techniques (37). To this end we write

$$c(\nu; \nu_0) = \sum_{i=0}^{i=N-1} r_i T_i \left(\frac{2\nu - 4 - \nu_0}{4 - \nu_0} \right), \quad (3.14)$$

where $T_i(z) = \cos(i \cos^{-1}(z))$ denotes the Chebyshev polynomial of order i , r_i are as yet undetermined coefficients and N is the truncation of the pseudo-spectral problem. We substitute this representation of the shock velocity into (3.13) and evaluate the resulting expression at collocation points for ν_B given by $\nu_j = (\nu_0 + 4 + (4 - \nu_0) \cos(j\pi/(N - 1)))/2$ ($1 \leq j \leq N - 2$), supplemented by the boundary conditions $c(0; 0) = 0$ and $c(4; 0) = -1$. This results in N coupled, nonlinear algebraic equations for the coefficients, r_i , which are solved numerically to determine the solution. We find that the solution is well resolved by 15 polynomials, with a residual less than 10^{-8} . Additional validation is provided by comparison with the series expansion (see Appendix A), which is formally valid for $\nu \ll 1$.

In Fig. 4(a), we plot the position of the shock, $x_s \equiv (2 - 3\nu/4)t_s$, as a function of time, determined by the hodograph techniques along with its position determined by the direct numerical integration of the governing equations. We note that the two approaches yield results that are virtually indistinguishable in this plot. Furthermore we note that the shock, x_s always lags the edge of the expansion fan, $x_r = -t$, but that $x_s \sim x_r$ as $t \rightarrow \infty$ (see inset of Fig. 4(a)). The time, $t_w(\nu)$, may be found from (3.11) given the

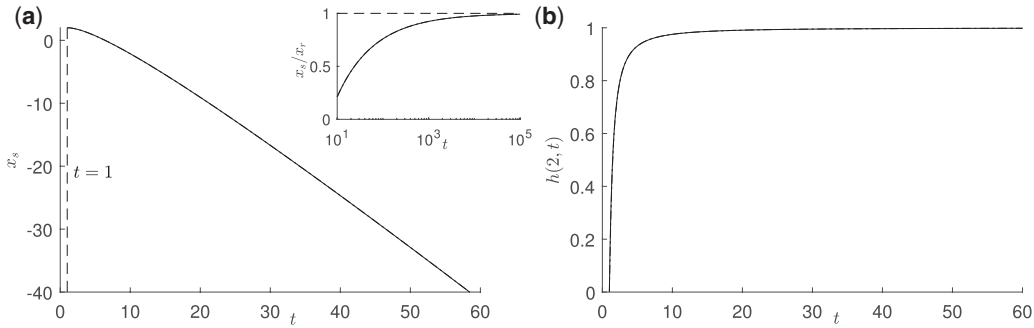


Fig. 4 (a) The position of the shock, x_s , (Inset: x_s/x_r) and (b) the fluid depth at the barrier, $h(2, t)$, as functions of time. In these plots, the results from the hodograph analysis are plotted with a solid line and the results from numerical simulation with a dotted-dash line; the curves are virtually indistinguishable. The shock is formed at $t = 1$ when the flow front first reaches the barrier and $h(2, t) = 0$ for $t \leq 1$.

solution for $c(v; 0)$ and hence we find the depth of the fluid layer at the barrier as a function of time, $h(2, t)$ (see Fig. 4(b)). The depth initially grows relatively rapidly, before progressively approaching its long term limit ($h \rightarrow 1$ as $t \rightarrow \infty$). Once again there is very close agreement between the results from the hodograph techniques and the direct numerical integration.

Having determined the shock velocity, $c(v)$, and thus the shock curve, (α_s, β_s) , in the hodograph plane (see Fig. 3), we may then evaluate $t(\alpha, \beta)$ and $x(\alpha, \beta)$ within the complex wave region, C_1 (see Fig. 2), which corresponds to the region in the hodograph plane between the shock curve and the impermeable barrier, $\alpha + \beta = 0$. To evaluate $t(\alpha, \beta)$, we integrate (2.13) around a closed curve $ODEF$ in the hodograph plane, where O is the origin, $D = (\alpha_s(v_D), \beta_s(v_D))$, $E = (\alpha, \beta)$ and $F = (-\beta, \beta)$ (see Fig. 3). From these coordinates, there are two important values of the parameter v , determined by $\alpha = \alpha_s(v_D)$ and $-\beta = \alpha_s(v_F)$. Then on integrating (2.13) around the closed curve $ODEF$ (see Fig. 3), we find

$$\begin{aligned}
 t(\alpha, \beta) = & \frac{1}{2} \left(\frac{\alpha - \beta_s(v_D)}{\alpha - \beta} \right)^{3/2} t_s(v_D) + \frac{1}{2} \left(\frac{-2\beta}{\alpha - \beta} \right)^{3/2} t_w(v_F) \\
 & - \int_0^{v_D} (-Va'_s + Ub'_s) dv + \int_0^{v_F} \frac{t_w(v)}{2} \left(\frac{\partial B}{\partial a} + \frac{\partial B}{\partial b} \right) \frac{da_s}{dv} dv.
 \end{aligned} \tag{3.15}$$

In the penultimate integral of (3.15), the Riemann function B and its derivatives are evaluated along the shock curve in the hodograph plane $(a, b) = (a_s, b_s)$, whereas in the final integral of (3.15) these functions are evaluated along the line $(a, b) = (a_s, -a_s)$, which corresponds to the barrier and are parameterised in terms of $a_s(v)$. The former arises from the integral along OD and the latter from FO . The solution for $x(\alpha, \beta)$ follows from $t(\alpha, \beta)$ using (2.10) and the boundary condition that $x = 2$ on $\alpha = -\beta$. Both $t(\alpha, \beta)$ and $x(\alpha, \beta)$ are straightforwardly evaluated using numerical quadrature. Given these functions, we may then calculate profiles of the flow depth and velocity as functions of distance along the channel at various instants of time. These are plotted in Fig. 5, along with the profiles computed from the numerical simulation of the nonlinear shallow water equations. It is notable that these profiles computed by the different approaches are in very close agreement, with

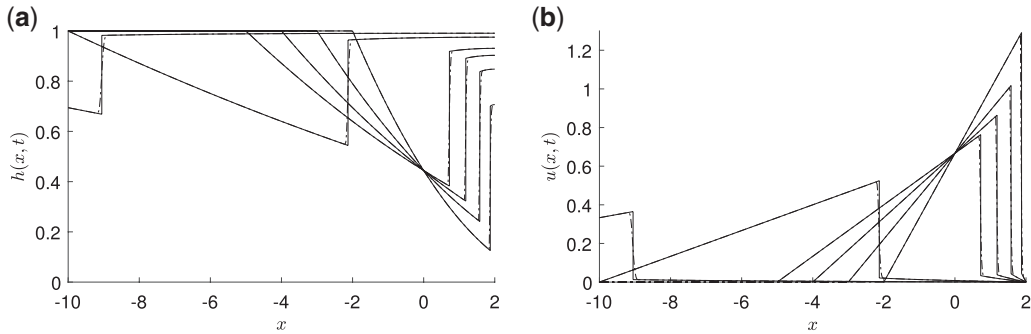


Fig. 5 (a) The depth of the fluid layer, h , and (b) the velocity, u , as functions of distance along the channel, x , at $t = 2, 3, 4, 5, 10$ and 20 . In these profiles, the hodograph results are plotted with a solid line and the numerical simulations with a dot-dashed line, although the two are virtually indistinguishable.

minor differences occurring close to the shock, which is spread over a few cells in the simulation results. These profiles illustrate that the flow generates an unsteady shock that propagates upstream, over which the depth of the flowing layer significantly increases and the velocity decreases (though still remaining in the positive streamwise direction). At late times, the jump in the dependent fields becomes smaller and the shock velocity tends to a unit upstream velocity ($c \rightarrow -1$).

4. Dam-break reflection with tailwaters ($h_0 > 0$)

The reflection of the flow when the dambreak collapses through a tailwater takes a more complicated form from section 3 because, during the initial phases at least, the incoming velocity and depth fields are uniform. This leads to additional regions in the characteristic plane (see Fig. 6) and a slightly amended analytical construction to determine the velocity of the reflected shock.

The front reaches the barrier at $t_{P1} = 2/V$ and a reflected shock is generated from $P_1 = (2, t_{P1})$ (see Fig. 6), separating the subsequent incoming flow in which $(u, h) = (u_f, h_f)$ corresponding to a uniform region U_2 , from a growing quiescent, uniform region adjacent to the barrier (denoted U_3). The shock velocity, c_3 , and depth of the fluid within the U_3 region, h_3 , are determined from the jump conditions (2.4): denoting $\mathcal{H} = h_3/h_f$, we deduce that

$$\frac{(1 - \mathcal{H})^2(1 + \mathcal{H})}{2\mathcal{H}} = \frac{u_f^2}{h_f} \quad \text{and} \quad c_3^2 = h_f \frac{(1 + \mathcal{H})}{2\mathcal{H}}. \quad (4.1)$$

Within this barrier-attached uniform region, U_3 , $\alpha = -\beta \equiv -\beta_3 \equiv 2\sqrt{h_3}$, because there is no flow (see Figs 6 and 8). We plot in Fig. 7 the dependence of the depth of the fluid layer, h_3 , and the reflected shock velocity, c_3 , as functions of the initial tailwater depth, determined from (4.1). As with the front velocity and depth of the Stoker flows (2.8)–(2.9), these reflected properties depend strongly on the tailwater depth: in particular, we find that

$$c_3 = -2^{1/4}h_0^{1/4} + \dots \quad \text{and} \quad h_3 = 2^{9/4}h_0^{1/4} + \dots \quad \text{when} \quad h_0 \ll 1. \quad (4.2)$$

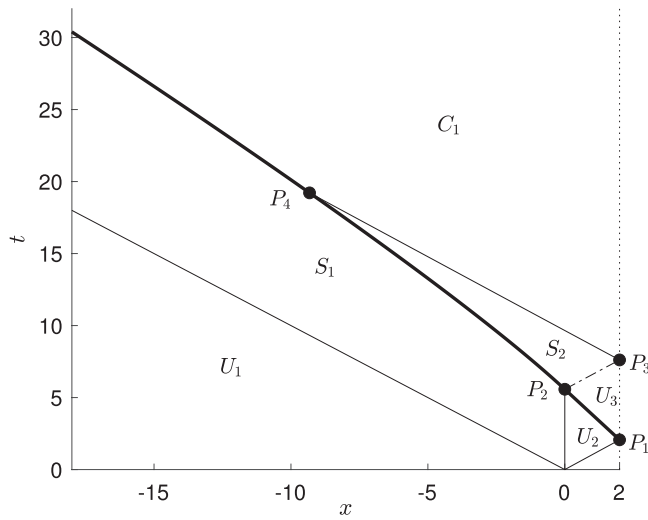


Fig. 6 The characteristic plane for the reflection of dam-break initial conditions with a tailwater ($h_0 = 0.1383$ for which $V_1 = 0$). The uniform, simple wave and complex wave regions are labelled, along with key points P_1 , P_2 , P_3 and P_4 in the characteristic plane. The trajectory of the shock is plotted with a thick solid line, α -characteristics with a dot-dashed line, β -characteristics with a thin solid line and the barrier ($x = 2$) with a dotted line.

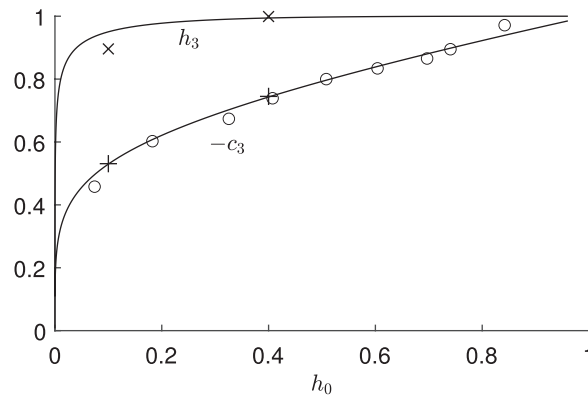


Fig. 7 The depth of the reflected fluid layer, h_3 , and the shock velocity, c_3 within the uniform region U_3 as a function of the tailwater depth after reflection from the barrier. Also plotted are experimental measurements from (12) for the reflected shock velocity, $-c_3$ (+) and the fluid depth h_3 (x) and from (11) for the reflected shock velocity, $-c_3$, (o).

Alongside the theoretical predictions, we plot experimental data extracted from (11) and (12) at locations that lie within the uniform region, U_3 , adjacent to the barrier, correcting a factor of $\sqrt{2}$ in the former (see Fig. 7). We also note that in order to compare the experimental measurements with this theory, we had to ensure the locations at which the flow hydrographs were taken lay within the uniform region, U_3 , which may be verified using the construction of the characteristic plane for each of the tailwater depths. In addition, we ensured that the effects of the backwall of the reservoir (that is its finite extent) had not influenced the motion; we assessed the latter by computing the reflected characteristic from the backwall of the reservoir (see sections 6 and (9)) and computing when it intersected with the shock reflected from the barrier at the end of the channel. The data plotted was only drawn from those locations and times at which the motion was not affected by the finite extent of the release. We observe that there is close agreement between the theoretical predictions and experimental measurements, even though there are reported free-surface waves close to the shock. This provides further confidence that the shallow water model accurately captures the motion.

The uniform region, U_3 , persists until the reflected shock first intersects the lead β -characteristic from the rarefaction fan (see Fig. 6). This occurs at position P_2 with coordinates (x_{P_2}, t_{P_2}) , where

$$(x_{P_2} - 2) = c_3(t_{P_2} - t_{P_1}) \quad \text{and} \quad x_{P_2} = \frac{(3\beta_* + 2)}{4}t_{P_2}, \quad (4.3)$$

where β_* is defined after (2.6). The uniform region, U_3 , is also bounded by the α -characteristic emanating from P_2 . This characteristic meets the barrier at location $P_3 = (2, t_{P_3})$, where

$$t_{P_3} \equiv t_{P_2} + \frac{2 - x_{P_2}}{\sqrt{h_3}}. \quad (4.4)$$

For $t > t_{P_2}$, we compute the coupled evolution of the reflected shock, which now separates two simple wave regions, S_1 and S_2 (see Fig. 6) and the $\beta = \beta_3$ characteristic that starts at P_3 and is denoted by $(x_3(\alpha), t_3(\alpha))$. The shock curve is a parametric function of the characteristic value of $\beta = 2 - \nu$ in the rarefaction fan, S_1 , with $\nu \geq 2 - \beta_*$, and satisfies (3.2) and (3.4). The characteristic curve, (x_3, t_3) , is a function of α in S_2 , which may also be treated as a parametric function of ν . Within the simple wave region, S_2 , α -characteristics are launched from the shock, propagate downstream and intersect the trajectory of the $\beta = \beta_3$ characteristic that emanates from P_3 . Thus, for an $\alpha = \hat{\alpha}$ characteristic, we find

$$x_3 - x_s = \frac{1}{4} (3\hat{\alpha} + \beta_3) (t_3 - t_s). \quad (4.5)$$

Finally, we note that the (x_3, t_3) characteristic on which $\beta = \beta_3$, given as a function of $\hat{\alpha}$, satisfies

$$\frac{dx_3}{d\hat{\alpha}} + \frac{1}{4}(\hat{\alpha} + 3\beta_3)\frac{dt_3}{d\hat{\alpha}} = 0. \quad (4.6)$$

From (4.5) and (4.6), we deduce that

$$\frac{dt_3}{d\nu} = \frac{3(t_3 - t_s)}{2(\beta_3 - \hat{\alpha})} \frac{d\hat{\alpha}}{d\nu} + \frac{2(c - \frac{1}{4}(3\hat{\alpha} + \beta_3))}{\beta_3 - \hat{\alpha}} \frac{dt_s}{d\nu}. \quad (4.7)$$

The system of differential equations (3.4) and (4.7) for $t_s(\nu)$ and $t_3(\nu)$ is completed by using the shock conditions (2.4) to relate flow states either side of the shock. These latter two conditions allow

$\hat{\alpha}$ and the shock velocity, c , to be determined as functions of v and then we may integrate the two coupled ordinary differential equations to find the trajectories of the shock and the β_3 -characteristic. A typical result is plotted in Fig. 6 for one value of the tailwater depth ($h_0 = 0.1383$). We find that eventually for some value of $v = \hat{v}_0$ that these two curves intersect; we find this location (x_{P_4}, t_{P_4}) and $\hat{\alpha} = \alpha_m$. (For example, for $h_0 = 0.1383$, this occurs at $P_4 : (x_{P_4}, t_{P_4}) = (-9.32, 19.21)$ and $\alpha_m = 1.9961$, see Fig. 6.) We note that in the limit of vanishing tailwater depth ($h_0 \rightarrow 0$), all the locations P_1, P_2, P_3 and P_4 coalesce to a single point $(x, t) = (2, 1)$ and we recover the characteristic structure of section 3.

To complete the solution for $t > t_{P_4}$ when $h_0 > 0$, we must account for the dynamics within the complex region C_1 , which is separated from the simple wave region S_1 by the reflected shock (see Fig. 6), and to this end we evaluate the integral (2.13) around closed curves in the hodograph plane. When there is a non-vanishing tailwater, the complex wave region, C_1 , is now separated from the reflected shock by the $\beta = \beta_3$ characteristic that connects P_3 to P_4 while $t_{P_3} < t < t_{P_4}$, but thereafter borders the shock (see Fig. 6). In the hodograph plane, the $\beta = \beta_3$ characteristic corresponds to the straight segment joining $G = (-\beta_3, \beta_3)$ and $H = (\alpha_m, \beta_3)$. The shock curves for $t > t_{P_4}$ is then given parametrically by $(\alpha_s(v), \beta_s(v))$ where $\hat{v}_0 \leq v \leq 4$, and as in section 3, the determination of this curve depends on the shock velocity, c , and its derivative, dc/dv . We introduce the following points in the hodograph plane: $J = (\alpha_s(v_J), \beta_s(v_J))$, which lies on the shock curve, and $K = (-\beta_s(v_J), \beta_s(v_J))$, which corresponds to the barrier location $(x = 2)$ at which the flow is reflected (see Fig. 8). Then integrating around the closed curve $GHJK$, made up of straightline segments GH, JK and KG and curved segment HJ , yields

$$0 = 2F(v_J) - 2I(v_J; v_0) - t_w(v_J) - \left(\frac{\alpha_s(v_J) - \beta_s(v_J)}{-2\beta_s(v_J)} \right)^{3/2} t_s(v_J), \tag{4.8}$$

where F arises from an integral along GH and is given by

$$F(v_J) = \int_{a=-\beta_3}^{\alpha_m} -V(a, \beta_3; -\beta_s(v_J), \beta_s(v_J)) da. \tag{4.9}$$

To close the problem we must determine an additional expression for t_w to eliminate it from (4.8). If $-\beta_s(v_J) > \alpha_m$ then as in section 3, we find a location $L = (\alpha_s(v_L), \beta_s(v_L))$ with $\alpha_s(v_L) + \beta_s(v_L) = 0$ and we integrate around the closed curve $GHLK$ (see Fig. 8(a)). This yields

$$0 = 2F(v_J) - 2I(v_L; v_0) + t_w(v_J) - \left(\frac{\alpha_s(v_L) - \beta_s(v_L)}{-2\beta_s(v_J)} \right)^{3/2} t_s(v_L). \tag{4.10}$$

Alternatively $-\beta_s(v_J) < \alpha_m$ we introduce $M = (-\beta_s(v_J), \beta_3)$ and integrate around GMK (see Fig. 8(b)) to establish

$$0 = 2\hat{F}(v_J) + t_w(v_J) - \left(\frac{-\beta_s(v_J) - \beta_3}{-2\beta_s(v_J)} \right)^{3/2} t_3(-\beta_s(v_J)), \tag{4.11}$$

where

$$\hat{F}(v_J) = \int_{a=-\beta_3}^{-\beta_s(v_J)} -V(a, \beta_3; -\beta_s(v_J), \beta_s(v_J)) da. \tag{4.12}$$

Then using either (4.10) or (4.11) (depending on whether $-\beta_s(v_J) > \alpha_m$ or $-\beta_s(v_J) < \alpha_m$), we eliminate t_w from (4.8) to find a single integral equation in terms of the unknown shock velocity

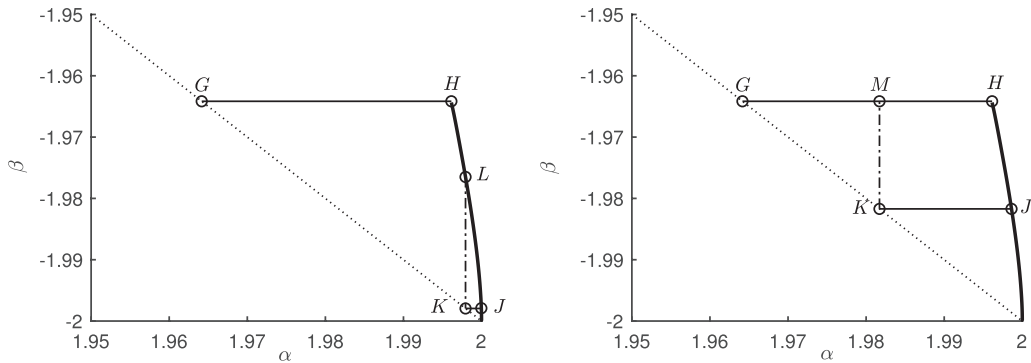


Fig. 8 The hodograph plane for the reflection of dam-break initial conditions with a tailwater ($h_0 = 0.1383$). The closed curves $GHJK$, $GHLK$ and GMK are used to determine the flow field within complex wave region, C_1 . The trajectory of the shock, (α_s, β_s) , is plotted with a thick solid line, α -characteristics are plotted with a dot-dashed line and β characteristics with a thin solid line. Also plotted is the line $\alpha = -\beta$ (dotted line), which corresponds to no flow at the barrier at the end of the domain.

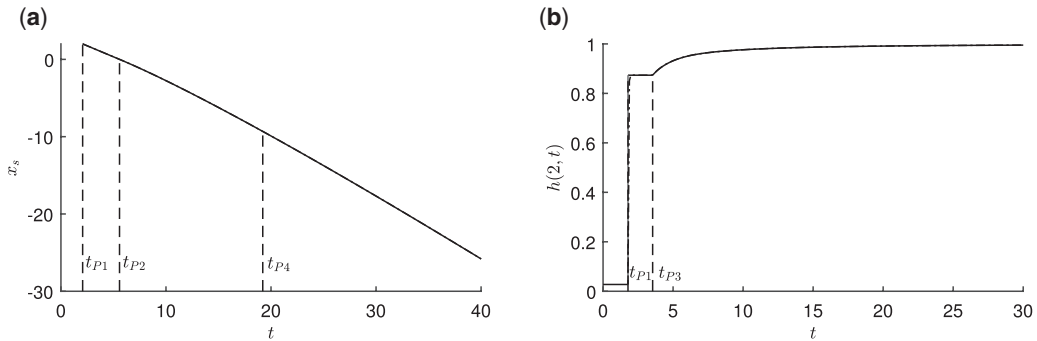


Fig. 9 (a) The position of the shock, x_s , and (b) the depth at the barrier, $h(2, t)$, as functions of time for $h_0 = 0.1381$. In these plots the results from the hodograph analysis are plotted with a solid line and the results from numerical simulation with a dotted-dash line; the curves are virtually indistinguishable. The shock is formed at $t = t_{P1}$, moves at constant velocity c_3 until $t = t_{P2}$ and separates the initial rarefaction, S_1 , from the complex wave region for $t > t_{P4}$. The depth of fluid at the barrier is equal to the tailwater depth, h_0 for $t < t_{P1}$ and then jumps to h_3 , before progressively increasing for $t > t_{P3}$.

c. We compute the solution for the shock velocity using the pseudo-spectral representation (3.14) in which we have substituted $v_0 = \hat{v}_0$. We evaluate at collocation points, solve for the coefficients and find a converged solution with 15 (or fewer) polynomials. The numerical solution for the shock velocity c allows the immediate evaluation of the time at the shock t_s and thus the position of the shock, x_s . This is plotted in Fig. 9(a).

We may also evaluate the depth of fluid at the barrier, $h(2, t)$ from t_w determined by (4.8) and plotted in Fig. 9(b). We observe the arrival of the front causes the fluid depth to jump first from the tailwater depth, h_0 to the constant depth, h_3 , which is maintained h_3 for some period. This corresponds

to the transition between region U_2 and U_3 (see Fig. 6). Thereafter the depth grows progressively and asymptotically approaches a unit value. Overlain on these quasi-analytical results are those from the direct integration of the shallow water equations. There is excellent correspondence between the two; the results are virtually indistinguishable in the figures, apart from during a few time-steps when the front first arrives at the barrier at $t = t_{P1}$ and when the solution changes with discontinuous gradient from a constant value to a temporally varying depth at $t = t_{P3}$.

5. Dissipation

Flows modelled using the nonlinear shallow water equations (2.1)–(2.2) only dissipate energy at discontinuities ('bores') or potentially at boundaries. For reflected dam-break flow, even though the initial state and the final state, attained asymptotically at sufficiently late times, are both quiescent layers of fluid of unit dimensionless depth, we anticipate dissipation because the motion generates a reflected shock. The difference in the total dimensionless energy per unit width of flowing material from the initial state is given by

$$\Delta E(t) = \int_{x_r}^2 \frac{1}{2} (u^2 h + h^2) dx - \left(h_0^2 - \frac{1}{2} x_r \right), \quad (5.1)$$

where where $x_r = -t$ denotes the upstream edge of the fan of β -characteristics generated by the initial release. The expression for ΔE corresponds to the total kinetic and potential energy in the region $x_r \leq x \leq 2$, minus the initial potential energy. The rate of change of ΔE is evaluated by differentiating (5.1) and using (2.1)–(2.2) to find that

$$\frac{d\Delta E}{dt} = -q \frac{(h^+ - h^-)^3}{4h^+ h^-}, \quad (5.2)$$

where h^\pm and u^\pm denote the depth and velocity fields upstream and downstream of a discontinuity and by mass conservation across the shock $q = h^+(u^+ - c) = h^-(u^- - c)$ (see, for example, (31)).

For flows with tailwater, a shock emerges as the motion approaches the barrier as well as when it is reflected and thus energy losses must take account of the motion of both. Since the forward propagating shock moves at constant velocity, V , it is straightforward to evaluate the energy loss when it reaches the barrier at $t = t_{P1}$,

$$\Delta E(t_{P1}) = -\frac{(h_f - h_0)^3}{2h_f}. \quad (5.3)$$

Note that there is no energy loss in the absence of a tailwater ($h_0 \rightarrow 0$), given the dependence of h_f on h_0 (2.9). Next there is dissipation during $t_{P1} < t < t_{P2}$ when the shock moves at constant velocity, c_3 . Thus, we find that

$$\Delta E(t_{P2}) - \Delta E(t_{P1}) = -c_3 \frac{(h_f - h_3)^3}{4h_f} (t_{P2} - t_{P1}). \quad (5.4)$$

The shock is subsequently located between two simple wave regions, S_1 and S_2 , and may be evaluated by integrating the temporally varying fields given by (3.4) and (4.7). Thus

$$\Delta E(t_{P3}) - \Delta E(t_{P2}) = - \int_{t_{P2}}^{t_{P3}} q \frac{(h^- - h^+)^3}{4h^- h^+} dt, \quad (5.5)$$

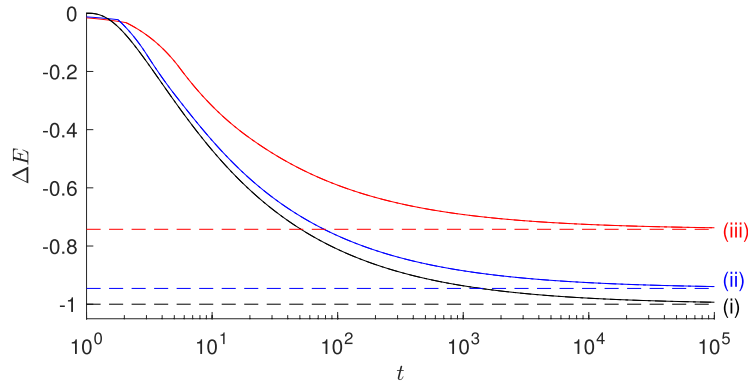


Fig. 10 The energy loss of reflected dam-break flow relative to the initial state, ΔE , as a function of time. The quasi-analytical hodograph result are plotted with a solid line, and the numerical results with a dot-dashed line ($t < 10^5$); the two are virtually indistinguishable. The late time asymptote ($\Delta E = -(1 - h_0)^2$) is also shown (dashed line). Three cases are plotted: (i) $h_0 = 0$ (black); (ii) $h_0 = 0.0275$ (blue); and (iii) $h_0 = 0.1383$ (red).

where h^- and h^+ are the depths of the fluid layer upstream and downstream of the shock, respectively. We note that in the absence of a tailwater, $t_{P4} = t_{P2} = t_{P1} = 1$ and there is no loss of energy until the final stage at which the shock separates the simple wave associated with the release and the complex wave region between the reflected shock and the barrier. In this regime the energy loss is conveniently evaluated in terms of the parameter, ν and using (5.2) is given by

$$\Delta E(t_s(\nu)) - \Delta E(t_{P3}) = \int_{\hat{v}_0}^{\nu} \frac{(4 - 2c - \nu)}{2048(\alpha_s - \beta_s)^2} \frac{3(\nu^2 - (\alpha_s - \beta_s)^2)^3 t_s}{(8 - 4c - 3\nu)} d\nu. \quad (5.6)$$

Thus the energy, ΔE , may be evaluated parametrically by numerical quadrature of (5.6) from the solution for $c(\nu)$ (which also gives α_s , β_s and t_s). We plot the energy loss, ΔE as a function of time in Fig. 10, noting that there is excellent agreement between the quasi-analytical determination through hodograph techniques (5.6) and the direct numerical evaluation (5.1), here plotted up to late times ($0 < t < 10^5$). The energy progressively decreases (see Fig. 10), as it must because physically realisable shocks are always dissipative. However, significant dissipation is not solely restricted to just the relatively early times when the amplitude of the shock is large, as measured by the relative magnitude of the changes in the depth of the flow across the shock. Instead there is systematic decrease and eventual approach to a constant asymptote (see Fig. 10).

Evaluating the dissipation at late times is a challenge for numerical simulations because the flow has spread over a large domain, all of which has to be stepped forward in time. In contrast, the quasi-analytical evaluation of dissipation is readily computed at late times because the solution for the shock velocity is computed as a function of ν and this enables the straightforward evaluation of (5.6). As plotted in Fig. 10, we have to extend to quite late times in order to realise the asymptotic value of the energy loss.

The late time limit may be analytically justified as follows (C. G. Johnson, Personal Communication, 2020). At late times, the fluid between the shock and the barrier ($x_s < x < 2$) forms an almost motionless layer of unit depth, whereas upstream the flow is given by (2.6). Then

conservation of fluid mass, or more precisely the absence of fluid, $1 - h$, over the domain implies that

$$2(1 - h_0) = \int_{x_r}^{x_s} 1 - \frac{1}{9} \left(2 - \frac{x}{t}\right)^2 dx + \int_{x_s}^2 (1 - h) dx \quad (5.7)$$

On the assumption that the fluid downstream of the bore is of unit depth to leading order so that

$$\int_{x_s}^2 (1 - h) dx \ll 1 \quad \text{when } t \gg 1, \quad (5.8)$$

a condition that we confirm using our hodograph and numerical solutions, we find from (5.7) that

$$2(1 - h_0) = x_s + \frac{t}{27} \left(2 - \frac{x_s}{t}\right)^3 + \dots \quad (5.9)$$

and therefore we deduce that

$$x_s = -t + \sqrt{6(1 - h_0)t} + \dots \quad (5.10)$$

Then to leading order the loss of energy is given by

$$\Delta E = \int_{x_r}^{x_s} \frac{1}{2} h^2 dx + \frac{1}{2}(2 - x_s) + \frac{1}{2}x_r - h_0^2 = -(1 - h_0)^2 + O(1/\sqrt{t}). \quad (5.11)$$

This asymptote is confirmed by the solution evaluated numerically and through hodograph techniques, and is plotted in Fig. 10. At late times, the fluid velocity is small and so the net change to the energy is dominated by the contributions to the potential energy; the region downstream of the lockgate is infilled with fluid, leading to an energy gain of $1 - h_0^2$, whereas fluid depth is reduced in the region $x_r < x < x_s$, leading to an energy loss of $2(1 - h_0)$. Combining these two yields the leading order result, $\Delta E = -(1 - h_0)^2$.

6. Maximum fluid depth at barrier from finite releases

We have shown above that the depth of the fluid layer at the barrier, $h(2, t)$, increases with time for dam-break releases from reservoirs of infinite extent (see, for example, Figs 4 and 9), and the motion asymptotically approaches unit depth at later times. However, if the reservoir is of finite length then the maximum depth, h_m , is less than unity and is achieved at a finite time ($h(2, t_m) = h_m$). In this section, focussing for simplicity on releases without tailwaters ($h_0 = 0$), we use the quasi-analytical solution to determine both the maximum depth and the time at which it is attained.

A finite extent reservoir introduces a backwall to the release, which is impermeable and at which the velocity must vanish. Denoting the dimensionless length of the reservoir by l (recall the dimensional streamwise distances are scaled by L where $2L$ is the distance from the lockgate to the barrier), the flow must satisfy

$$u(-l, t) = 0. \quad (6.1)$$

Fluid in the reservoir is initially at rest and remains so until the arrival of the rearmost β -characteristic from $x = 0$. Thus the flow is not affected by the backwall condition (6.1) for $t < l$, but thereafter

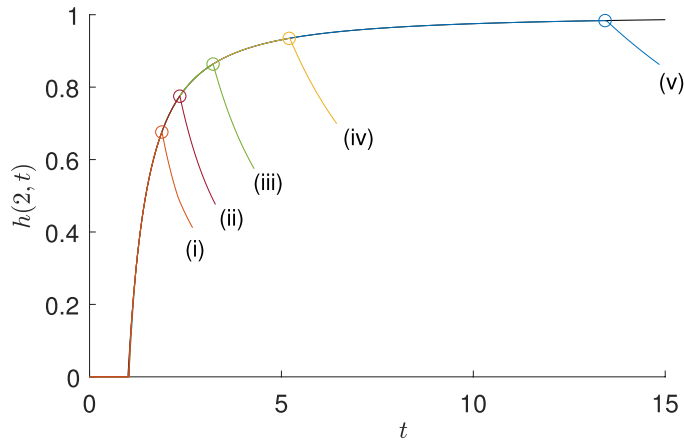


Fig. 11 The fluid depth at the barrier, $h(2, t)$, as a function of time for reservoir lengths: (i) $l = 0.31$; (ii) $l = 0.52$; (iii) $l = 0.93$; (iv) $l = 1.90$ and (v) $l = 6.00$. The plotted symbol represents the instance at which the depth reaches its maximum value. Also plotted is the fluid depth for an unbounded reservoir, calculated in section 3.

the depth at the backwall, $h(-l, t)$ begins to decrease and the rear-most β -characteristic is reflected to generate a forward-propagating α -characteristic. It is this forward-propagating characteristic that conveys the presence of the backwall and its arrival at $x = 2$ is associated with the maximum fluid depth at the barrier. The position of the reflected α -characteristic on which $\alpha = 2$, is straightforward to determine from (2.11) and is given parametrically by

$$t_c(\beta) = \frac{8l}{(2 - \beta)^{3/2}} \quad \text{and} \quad x_c(\beta) = \frac{2l(2 + 3\beta)}{(2 - \beta)^{3/2}}. \quad (6.2)$$

(see (9)). This characteristic intersects the shock at $\beta = 2 - \bar{v}$, where

$$t_s(\bar{v}) = \frac{8l}{\bar{v}^{3/2}}, \quad (6.3)$$

which is an algebraic equation for \bar{v} that is solved numerically. Given \bar{v} , we may evaluate $\alpha_s(\bar{v})$, which immediately gives $h_m = \alpha_s(\bar{v})^2/4$, while $t_m = t_w(\bar{v})$ (and evaluated from (3.11)).

We plot the depth of fluid at the barrier, $h(2, t)$, as a function of time for various reservoir lengths (Fig. 11) and note that its evolution follows a universal curve until reaching a maximum value. As described above, the universal behaviour follows the flow reflection for an unbounded reservoir and the maximum depth is attained when the first characteristic reflected from the backwall reaches the barrier; the numerically computed flow depth then decreases quite rapidly. We plot the maximum depth, h_m , and the time, t_m as a function of the dimensionless reservoir length, l , (Fig. 12), showing excellent agreement between the numerically computed maximum fluid depths from simulations with a wide range of reservoir lengths. When the reservoir is long ($l \gg 1$), the maximum depth asymptotes to unity, which recovers the result for infinite reservoirs. This arises because the rearmost β -characteristic from the initial fan is only reflected by the backwall at relatively late times and thus the flow has evolved for a considerable period without being influenced by the backwall.

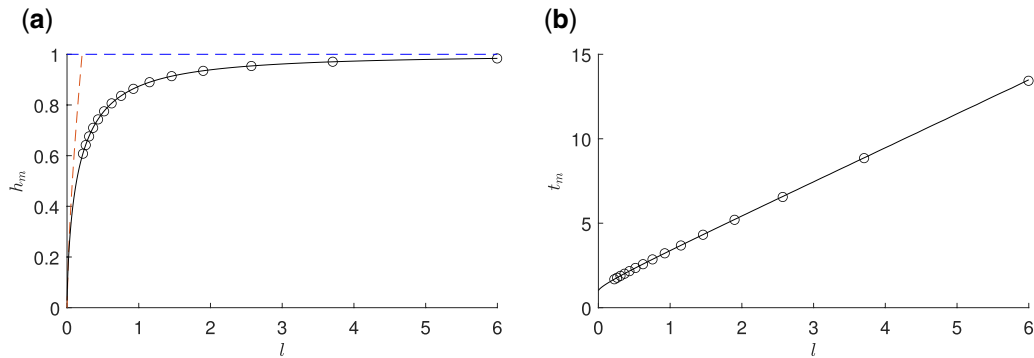


Fig. 12 (a) The maximum fluid depth at the barrier, h_m and (b) the time, t_m , at which it is attained functions of the dimensionless reservoir length (solid lines). Also plotted are the results from numerical simulations (circles). The asymptotic values for short ($l \ll 1$) and long ($l \gg 1$) reservoirs are plotted with dashed lines.

Conversely when $l \ll 1$, the reflection from the backwall occurs at very early times and the maximum depth is much less than unity. Using (A.7) and (A.5) to provide expansions for t_s and h when $\bar{v} \ll 1$, we deduce that to leading order

$$h_m = 8^{1/2} l^{2/3} + \dots \quad (6.4)$$

These results for h_m are of interest because they provide the height of the barrier that cannot be overtopped by a finite release.

7. Conclusion

In this investigation, we have comprehensively analysed the unsteady interaction of dam-break flow with an immovable barrier. The key features are that the reflection initiates an upstream propagating bore, that between the bore and the barrier the fluid deepens and flows slowly and that energy is progressively dissipated by the bore, with the energy loss tending to a constant at long times. Indeed, it is surprising that the energy loss only attains its asymptote on such long timescales. Our methods have combined quasi-analytical results for the nonlinear shallow water equations based upon their hodograph transformation, with direct numerical simulations of the governing system. The results from the two approaches are in excellent agreement, apart from within a few numerical cells surrounding the discontinuities of the flow, thus confirming the accuracy and utility of them both. We have shown how the motion is altered by the presence of a tailwater, leading to a more complex interaction with the barrier, but nevertheless, the same methods can be employed to calculate the motion. We contend that the identification of regions in the characteristic and hodograph planes aids understanding of the behaviour of the flow and the development of nonlinear features, such as bores.

The growth of the depth of fluid adjacent to the reflecting barrier is another key output from this analysis and enables the calculation of the hydrostatic force exerted on the barrier. This could be used to assess when flow-induced damage would occur, potentially altering or mobilising the reflector, either of which would affect the oncoming flow. Moreover, it is vital to determine the fluid depth in

order to assess whether the barrier could be over-topped by the release—and thus to judge efficacy of bunds that are used to contain spillages of potentially hazardous materials. We have also shown how to compute the maximum depth of the flow at the barrier attained by a finite release using the quasi-analytical solution and demonstrated that it is associated with the first reflected characteristic from the backwall. Importantly, a naive estimate of the maximum depth based solely on volume conservation would indicate a maximum fluid depth of $l/(l+2)$, but this is always less than, and sometimes much less than, h_m , because the flow generates a bore upon reflection and a fluid layer adjacent to the barrier that deepens rapidly.

Finally, we comment that this study provides further evidence of the effectiveness of numerical algorithms developed by Kurganov *et al.* (27) for integrating nonlinear hyperbolic systems. Furthermore, the dynamics calculated here through semi-analytical methods form a quite severe test of the efficacy of the numerical algorithms to capture bore generation and its long term evolution.

Acknowledgments

A. J. Hogg acknowledges the financial support of Natural Environmental Research Council, UK (NE/S00274X/1) and E. W. G. Skevington acknowledges the support of Engineering and Physical Sciences Research Council, UK (EP/M506473/1). The authors also thank two anonymous reviewers for their insightful comments on an earlier version of this article.

APPENDIX A

Series expansion for the reflected dam-break ($h_0 = 0$)

We examine dam-break reflection during the initial phases of its evolution (see section 3). This problem was first analysed asymptotically by (21); here, we adopt a different technique, which is arguably more straightforward and is readily extended to higher asymptotic orders. The new approach introduces the new independent variables given by

$$\xi = \frac{2-x}{2-x_s(t)} \quad \text{and} \quad \nu = \frac{4(2t-x_s(t))}{3t}. \quad (\text{A.1})$$

These variables correspond to a rescaled spatial coordinate, ξ , within the region between the shock ($\xi = 1$) and the barrier ($\xi = 0$), and a nonlinear time, ν . We note that $2-\nu$ is the value of the β -characteristic from the rarefaction fan (region S_1) that intersects the shock, the parametric position of which is given by $(x_s(\nu), t_s(\nu))$. The governing equations, (2.1) and (2.2), are then transformed to

$$\frac{d\nu}{dt} \frac{\partial h}{\partial \nu} + \frac{\xi}{2-x_s} \frac{dx_s}{dt} \frac{\partial h}{\partial \xi} - \frac{1}{2-x_s} \frac{\partial}{\partial \xi} (uh) = 0, \quad (\text{A.2})$$

$$\frac{d\nu}{dt} \frac{\partial u}{\partial \nu} + \frac{\xi}{2-x_s} \frac{dx_s}{dt} \frac{\partial u}{\partial \xi} - \frac{u}{2-x_s} \frac{\partial u}{\partial \xi} - \frac{1}{2-x_s} \frac{\partial h}{\partial \xi} = 0. \quad (\text{A.3})$$

The boundary condition is one of no flow at the barrier, namely $u(\xi = 0) = 0$, while at the shock ($\xi = 1$), we enforce the jump conditions (2.4), matching to the dam-break solution upstream of it (2.6). By (A.1), the position of the shock is given by $x_s = 2t - 3\nu t/4$ and thus the shock velocity is given by

$$c \equiv \frac{dx_s}{dt} = 2 - \frac{3}{4}\nu - \frac{3}{4}t \frac{d\nu}{dt}. \quad (\text{A.4})$$

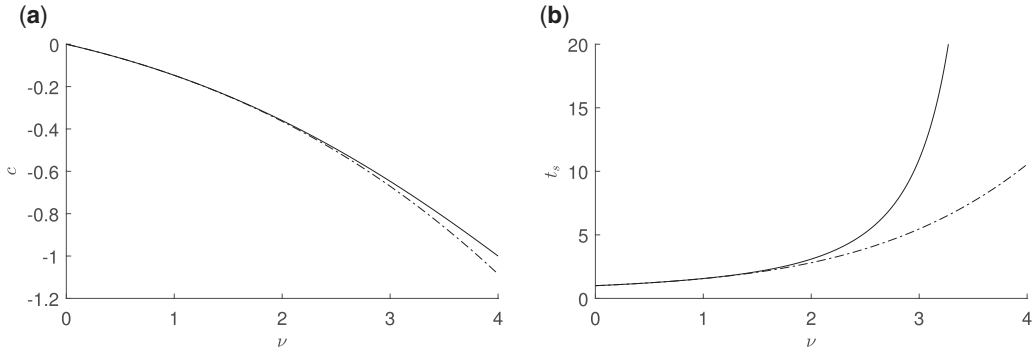


Fig. A.1 (a) The shock velocity, c , and (b) the time, t_s , as functions of the value of the upstream characteristic variable, $\nu = 2 - \beta$. In these plots the hodograph expression is plotted with a solid line and the asymptotic expression (A.7) and (A.8) with a dot-dashed line.

We expand time, t , and the dependent variables as regular series in integer powers of ν , substitute into (A.2) and (A.3) and balance terms of the same order of ν . In this way we find

$$h = \frac{\nu\sqrt{2}}{2} + \frac{\nu^2}{288}(4 - 36\sqrt{2} - \xi^2) + \frac{\nu^3}{124416}(-5\sqrt{2}\xi^4 - (22\sqrt{2} - 54)\xi^2 + 918 + \frac{819}{4}\sqrt{2}) + \dots \quad (\text{A.5})$$

$$u = \frac{\nu\sqrt{2}\xi}{24} + \frac{\nu^2\xi}{10368}(5\xi^2 - 162\sqrt{2} + 37) + \frac{\nu^3\xi}{5971968}(50\sqrt{2}\xi^4 + (170\sqrt{2} + 360)\xi^2 + 10872 - 14311\sqrt{2}) + \dots, \quad (\text{A.6})$$

$$t = 1 + \frac{3\nu}{8} + \frac{\nu^2(18 - \sqrt{2})}{128} + \frac{\nu^3(5854 - 864\sqrt{2})}{110592} + \frac{\nu^4}{10616832}(215136 - 55493\sqrt{2}) + \dots \quad (\text{A.7})$$

$$c = -\frac{\nu\sqrt{2}}{12} - \frac{\nu^2(13 + 54\sqrt{2})}{3456} - \frac{\nu^3(36 + 1073\sqrt{2})}{497664} + \dots \quad (\text{A.8})$$

Note that (A.4) enables the series solution for $t(\nu)$ to be determined up to $O(\nu^4)$ using the series truncated at $O(\nu^3)$ for the other dependent variables. The depth of fluid downstream of the shock therefore grows initially linearly with time after impact ($t - 1$), and is spatially invariant to leading order. The velocity field, meanwhile, is quite weak and varies linearly with distance from the barrier.

The solutions for the shock velocity, $c(\nu)$ and the time, $t_s = t(\nu)$ determined by the hodograph techniques in section 3 are plotted in Fig. A.1 along with their asymptotic representations (A.5)–(A.8). We observe that these series solutions closely match the complete solution for the shock velocity for $\nu < 2.2$, and that t_s is quite accurately captured when $t_s < 2$.

References

1. J. C. Martin and W. J. Moyce, Part IV: An experimental study of the collapse of liquid columns on a rigid horizontal plate, *Proc. R. Soc. Lond. A* **244** (1952) 312–324.

2. R.F. Dressler Comparison of theories and experiments for the hydraulic dam-break wave. Proc. Intl Assoc. of Scientific Hydrology Assemblée Générale, Rome, Italy, Vol. 3 (1954), 319–328.
3. G. Lauber and W. H. Hager, Experiments to dambreak wave: horizontal channel, *J. Hydr. Res.* **36** (1998) 291–307.
4. M. Pilotti, A. Maranzoni, M. Tomirotti and G. Valerio, 1923 Gleno dam break: case study and numerical modelling, *J. Hyd. Eng.* **137** (2011) 480–492.
5. A. Ritter, Die Fortpflanzung der Wasserwellen, *Zeitschrift des Vereines Deutscher Ingenieure* **36** (1892) 947–954.
6. J.J. Stoker, Water Waves, the Mathematical Theory with Applications, Vol. 4 Pure and Applied Mathematics (John Wiley and Sons Ltd, 1957).
7. R. F. Dressler, Hydraulic resistance effect upon the dam-break functions, *J. Res. Nat. Bur. Stand.* **49** (1952) 217–225.
8. A. J. Hogg and D. Pritchard, The effects of drag on dam-break and other shallow inertial flows, *J. Fluid Mech.* **501** (2004) 179–212.
9. A. J. Hogg, Lock-release gravity currents and dam-break flows, *J. Fluid Mech.* **569** (2006) 61–87.
10. B. Hunt, An inviscid dam-break solution, *J. Hydr. Res.* **25** (1987) 313–327.
11. V. I. Bukreev, Force action of discontinuous waves on a vertical wall, *J. Appl. Mech. Theor. Phys.* **50** (2009) 278–283, 2009.
12. S. Kocaman and H. Ozman-Cagatay, Investigation of dam-break induced shock waves impact on a vertical wall, *J. Hydrol.* **525** (2015) 1–12.
13. L. Lobovsky, E. Botia-Vera, F. Castellana, J. Mas-Soler and A. Souto Iglesias, Experimental investigation of dynamic pressure load during dam break, *J. Fluids Struct.* **48** (2014) 407–434.
14. F. Aureli, S. Dazzi, A. Maranzoni, P. Mignosa and R. Vacondio, Experimental and numerical evaluation of the force due to the impact of a dam-break wave on a structure, *Adv. Water Res.* **76** (2015) 29–42, 2015.
15. C. Yang, B. Lin, C. Jiang and Y. Liu, Predicting near-field dam-break flow and impact force using a 3D model, *J. Hydr. Res.* **48** (2010) 784–792.
16. H. Ozman-Cagatay and S. Kocaman, Dam-break flow in the presence of obstacle: experiment and CFD simulation, *Eng. Appl. Comput. Fluid Mech.* **5** (2011) 541–552.
17. S. Soares-Frazaao and Y. Zech, Experimental study of dam-break flow against an isolated obstacle, *J. Hydr. Res.* **45** (2007) 27–36, 2007.
18. S. Soares-Frazaao and Y. Zech, Dam-break flow through an idealised city, *J. Hydr. Res.* **46** (2008) 648–658.
19. A. Issakhov, Y. Zhandaulet and A. Nogaeva, Numerical simulation of dam break flow for various forms of the obstacle by VOF method, *Int. J. Multiphase Flow* **109** (2018) 191–206.
20. C. Di Cristo, M. Greco, M. Iervolino and A. Vacca, Interaction of a dam-break wave with an obstacle over an erodible floodplain, *J. Hydroinformatics* **22** (2020) 5–19.
21. H. P. Greenspan and R. E. Young, Flow over a containment dyke, *J. Fluid Mech.* **87** (1978) 179–192.
22. A. M. Thyer, I. L. Hirst and S. F. Jagger, Bund overtopping - the consequences of catastrophic tank failure, *J. Loss Prev. Process Ind.* **15** (2002) 357–363.
23. D. M. Webber and M. J. Iving, Modelling bund overtopping using Shallow Water Theory, *J. Loss Prev. Process Ind.* **23** (2010) 662–667.
24. A. J. N. Goater and A. J. Hogg, Bounded dam-break flows with tailwaters, *J. Fluid Mech.* **686** (2011) 160–186.
25. M. Antuono and A. J. Hogg, Run-up and backwash bore formation from dam-break flow on an inclined plane, *J. Fluid Mech.* **640** (2009) 151–164.
26. E. W. G. Skevington and A. J. Hogg, Unsteady draining of reservoirs over weirs and through constrictions, *J. Fluid Mech.* **882** (2020) A9.

27. A. Kurganov, S. Noelle and G. Petrova, Semi-discrete central-upwind schemes for hyperbolic conservation laws and Hamilton-Jacobi equations, *SIAM J. Sci. Comput.* **23** (2001) 707–740.
28. K. P. Stanyukovich, *Unsteady Motion of Continuous Media* (Pergamon Press 1960).
29. H. P. Greenspan and D. S. Butler, On the expansion of a gas into vacuum, *J. Fluid Mech.* **13** (1962) 101–119.
30. D. H. Peregrine, Equations for water waves and the approximations behind them. *Waves on Beaches and resulting sediment transport*, chapter 3 (ed. R. Meyer; Academic Press 1972) 95–121.
31. G.B. Whitham, *Linear and nonlinear waves* (John Wiley & Sons, 1974).
32. A. J. Hogg, T. E. Baldock and D. Pritchard, Overtopping a truncated planar beach, *J. Fluid Mech.* **666** (2021) 521–553.
33. P. R. Garabedian, *Partial Differential Equations* (Chelsea Publishing, 1986).
34. E. W. G. Skevington, A well balanced reconstruction with bounded velocities and low-oscillation slow shocks for the shallow water equations. *arXiv:2106.11256* (2021)b.
35. E. W. G. Skevington, The implementation of a broad class of boundary conditions for non-linear hyperbolic systems. *arXiv:2106.11262* (2021)b.
36. C. Shu and S. Osher, Efficient implementation of essentially non-oscillatory schemes, *J. Comput. Phys.* **77** (1988) 439–471.
37. J. P. Boyd *Chebyshev and Fourier Spectral Methods*, Second Edition (Dover, 2001)